# A model invalidation procedure for wave energy converters with experimental assessment and implications for control

Control Engineering Practice 143 (2024) 105778

Contents lists available at ScienceDirect

Control Engineering Practice

journal homepage: www.elsevier.com/locate/conengprac

# A model invalidation procedure for wave energy converters with experimental assessment and implications for control

Demián García-Violini [a,b,c,*], Yerai Peña-Sanchez [d,c], Nicolás Faedo [e,c], Fernando Bianchi [a,f], John V. Ringwood [c]

[a] CONICET, Argentina
[b] Departamento de Ciencia y Tecnología, Universidad Nacional de Quilmes, Bernal, Argentina
[c] Centre for Ocean Energy Research (COER), Department of Electronic Engineering, Maynooth University, Co. Kildare, Ireland
[d] Euskal Herriko Unibertsitatea (EHU/UPV), Bizcaia, Spain
[e] Marine Offshore Renewable Energy Lab., Department of Mechanical and Aerospace Engineering, Politecnico di Torino, Italy
[f] Instituto Tecnológico de Buenos Aires, Ciudad Autónoma de Buenos Aires, Argentina

ARTICLE INFO

*Keywords:*
Model invalidation
Model validation
WECs
Uncertainty
Robust control
Control oriented models

ABSTRACT

Model invalidation is the process of testing assumptions of a dynamical model by comparing simulated responses with experimental data, considering any discrepancies as evidence that the model may be invalid. In this study, a model invalidation methodology is presented, to obtain robust control oriented models for wave energy converters (WECs). In particular, this methodology can deal separately with dynamical uncertainty and external noise in experimental data sets. To this end, considering linear system theory, this study proposes a methodology for building input–output data sets for WEC systems, via a two-stage approach. Model invalidation results are analysed statistically, and the practical implications of considering dynamical uncertainty in WEC system models are discussed in terms of control performance, specifically absorbed energy. As indicated by the analysis and results presented in this study, failure to include dynamic uncertainty in the analysis can lead to performance overestimation. The importance of a good dynamical description for accurate estimation of experimental control performance is highlighted. Finally, this study emphasises the need for closed-loop controllers for WEC systems that can simultaneously maximise energy and guarantee robust stability, an area currently lacking within the WEC literature.

## 1. Introduction

Ocean waves are one of the most powerful natural forces on Earth, capable of generating vast amounts of energy that could prove instrumental in halting and reversing the damaging effects of climate change (Guo & Ringwood, 2021). Thus, harnessing the power of the ocean has the potential to become a key component in a carbon-free energy generation scheme, satisfying global energy needs while mitigating environmental harm caused by carbon-based energy sources. Although wave energy converter (WEC) technology has been under development for several decades, becoming markedly more attractive during the past years, commercial viability still poses significant challenges (Ringwood, Bacelli, & Fusco, 2014).

To achieve commercial success of WECs, several considerations have been well established and accepted within the R & D community. In particular, dynamical system theory plays a crucial role, to effectively deal with, for example, the interaction of complex mechanical, electrical, estimation, forecasting, and control systems. Wave energy systems can be highly nonlinear and time-varying, posing significant challenges for the design, operation, and control of WECs. Consequently, precise dynamical descriptions of WEC systems represent a fundamental component in achieving effective designs, mainly focusing on commercial competitiveness. Within a dynamical theory framework, there are several aspects that differentiate WEC systems from other engineering applications, particularly from an automatic control point of view. In particular, WEC systems are affected by the so-called modelling paradox phenomenon (Windt, Faedo, Penalba, Dias, & Ringwood, 2021), arising from the use of linear models during the design stage of, for example, controllers or estimators, while, as a consequence of the control action, during operation, the system motion is exaggerated beyond the linear range. The resulting model/controller mismatch can result, at the very least, in significant energy conversion performance reduction.

* Corresponding author at: Departamento de Ciencia y Tecnología, Universidad Nacional de Quilmes, Bernal, Argentina.
*E-mail addresses:* ddgv83@gmail.com (D. García-Violini), yerai.pena@ehu.eus (Y. Peña-Sanchez), nicolas.faedo@polito.it (N. Faedo), febianchi@itba.edu.ar (F. Bianchi), john.ringwood@mu.ie (J.V. Ringwood).

https://doi.org/10.1016/j.conengprac.2023.105778
Received 11 May 2023; Received in revised form 11 October 2023; Accepted 4 November 2023
Available online 19 November 2023

Several steps can be taken into account to obtain useful dynamical descriptions. In particular, to overcome the above-mentioned impediments, the experimental stage represents a key step in the development of efficient and effective WEC systems, beyond simplifications made for its dynamical description. Similarly, to achieve more accurate dynamic models, recent studies have introduced methodologies to quantify uncertainty in WEC system descriptions (Farajvand, García-Violini and Ringwood, 2023; Farajvand, García-Violini, Windt, Grazioso, & Ringwood, 2021; Farajvand, Grazioso, García-Violini and Ringwood, 2023) which, although relying on linear assumptions and descriptions, are able to implicitly incorporate information on more complex dynamics (non-linearities, for example). In particular, Farajvand, García-Violini et al. (2023), Farajvand, Grazioso et al. (2023) and Farajvand et al. (2021) provide methodologies for describing deviations between simulated model responses and experimental (or high fidelity simulation) responses. These deviations can be caused by, for example, specific hydrodynamic effects, numerical issues due to the simulation environment, or measurement noise (experimental). However, in Farajvand, García-Violini et al. (2023), Farajvand, Grazioso et al. (2023) and Farajvand et al. (2021) numerical issues, external noise, and dynamical uncertainty, are not distinguished, which, from the robust control perspective, can significantly impact on, for instance, robust stability.

Generally, to link experimental (high fidelity simulation) and dynamic descriptions (models), obtained either by physical (first principles) modelling or identification methods using system data, a validation stage is usually performed, where simulated responses are compared with those experimentally obtained. However, based on the *Falsifiability* theory by Popper (2005), the term *'model validation'* can be misleading, since it is not possible to fully validate a model based on a limited number of experiments. In contrast, if a single experiment is not aligned with the model (and its assumptions), it can be considered invalid. Conversely, when an experimental response verifies the assumptions considered for the model, it can be said that *the experiment* ***does not invalidate*** *the model* and its hypotheses. Based on this theoretical and philosophical paradigm, a validation framework denoted *'model invalidation'* has been presented in the literature of dynamical and control systems (see for example Smith (1990), Smith and Doyle (1989) and Smith, Dullerud, Rangan, and Poolla (1997)), where dynamic perturbations and external noise (both unknown but bounded) can be separately represented. In particular, a model invalidation framework is particularly suitable for tackling robust control design problems, such us $\mathcal{H}_\infty$ (Sanchez-Peña & Sznaier, 1998), and its implications on robust stability and performance (Garcia-Violini & Ringwood, 2021). In particular, model invalidation has been applied in a number of different application areas (Anderson & Papachristodoulou, 2009; Beven & Lane, 2019; Bianchi, Moscoso-Vásquez, Colmegna, & Sánchez-Pena, 2019; Livstone, Dahleh, & Farrell, 1994; Vrachimis, Timotheou, Eliades, & Polycarpou, 2021), while the fundamental results, for linear-time invariant (LTI) systems, have been extended to areas, such as linear-parameter varying (LPV) systems (Sznaier & Mazzaro, 2003), fault detection (Harirchi & Ozay, 2018), and for system identification (Bianchi & Sánchez-Peña, 2010b), in LTI, LPV, and switched system frameworks. In particular, Section 3 presents a thorough discussion of model invalidation, including a comparison with traditional validation approaches, from the perspective of WEC systems. From an overall perspective, in the broader modelling community, model 'verification and validation', often abbreviated as V & V, plays a key role in ensuring the accuracy and reliability of mathematical models. Verification confirms the correct implementation of mathematical models into numerical simulations, while validation extends to demonstrating the predictive capacity of the model, within defined regions of application. This article delves deeper into the validation process, specifically contrasting it with model invalidation, providing a finer and more comprehensive understanding of model assessment. While validation is critical to confirm the predictive capabilities of a model, model invalidation, as explored in this study, offers the advantage to not only verify the 'correctness' of a model, but also identify its limitations and areas where it may fail.

Using a wide set of experimental data, and considering linear system theory, this study focusses on model invalidation and control performance for WEC systems, separated into two stages.

Firstly, an invalidation procedure is carried out using experimental datasets obtained using: (i) three nominal models, based on first principles , system identification, and by manual adjustment of the moment of inertia, respectively; for (ii) four sea-states; and (iii) different dynamical perturbation assumptions. In addition, the invalidation procedure, rather than giving a binary indication (*not-invalidated* or *invalidated*), as generally used in the literature, takes advantage of the full amount of available data, performing a statistical global analysis to reduce conservativeness. Thus, statistical estimates for dynamical perturbation and noise bounds are obtained in the first step. It is worth emphasising that the methodology for conducting experiments, specifically in the context of WECs, requires a two-stage signal acquisition procedure, due to the intrinsic nature of the application. This study discusses the impact of this two-step experimental acquisition methodology on the final results, which can be considered as an additional source of exogenous uncertainty.

Secondly, including incorporation of the obtained estimates of dynamical uncertainty and noise bounds in the model description, two well-established control methodologies are assessed. In particular, a proportional–integral (PI) control, also referred to as a reactive controller, and a LiTe-Con controller (García-Violini, Peña-Sanchez, Faedo and Ringwood, 2020), both based on the impedance-matching principle (García-Violini, Faedo, Jaramillo-Lopez and Ringwood, 2020), are assessed. The results show that, when uncertainty and noised are included in the dynamical description of the system, a significant amount of power absorption variability can be obtained, which can lead to overestimation of performance. Furthermore, stability issues, for closed-loop forms, are also discussed as a consequence of considering a dynamical description with a perturbation model.

To summarise, in this study:

- A two-stage method for input–output dataset acquisition is proposed,
- an invalidation analysis framework is introduced for WEC systems,
- a statistical approach is considered to globally analyse the invalidation results, and
- the impact on control performance of considering a dynamical model with perturbations is discussed.

The remainder of this paper is structured as follows. In Section 2, the standard modelling framework necessary to describe and analyse the dynamical behaviour of WEC systems is introduced. Section 3 provides a detailed account of the theoretical basics of model invalidation, with particular emphasis on practical considerations. Methodological guidelines for building input–output datasets in WEC systems are presented and discussed in Section 4. In Section 5, the application of the presented model invalidation framework is demonstrated using experimental data. Based on the results from Section 5, Section 6 describes the implementation of different control methodologies and shows the consequences, in terms of power absorption, of considering robust-control oriented models. Finally, Section 7 summarises the main findings and draws conclusions.

## 2. WECs: modelling framework

The dynamic model of a WEC system, which characterises the motion of a floating body or even arrays of WECs resulting from the action of hydrodynamic forces, is defined using the so-called Cummins' equation, a well-established and widely adopted theoretical framework (Cummins, 1962). Using this formulation, which is essentially based on Newton's second law, the dynamic behaviour of a general

WEC system can be described. In this study, without any loss of generality, a rotational WEC with a single degree-of-freedom is considered, consistent with the WEC prototype considered in Section 5. The model is hence defined as:

$$\left(I + A_\infty\right)\ddot{\theta}(t) = \tau(t) - \tau_r(t) - \tau_h(t) - \tau_u(t), \tag{1}$$

where $I$ is the body inertia, $\theta$, $\dot{\theta}$ and $\ddot{\theta}$ denote the angular position, velocity, and acceleration of the device, respectively. The radiation torque is defined as $\tau_r(t) = k_r(t) * \dot{\theta}(t)$, where $*$ denotes a convolution integral operation and $k_r(t)$ the radiation torque impulse response. The restoring (buoyancy) force is denoted as $\tau_h(t) = s_h\theta(t)$, where $s_h$ indicates the hydrostatic stiffness, and $\tau_u(t)$ and $\tau(t)$ are the control torque, applied by means of the power take-off (PTO) system, and the excitation torque, respectively. In Eq. (1), $A_\infty = \lim_{\omega\to+\infty} A_r(\omega)$ is the added mass at infinite frequency, where $A_r(\omega)$ and $B_r(\omega)$ are the radiation added-mass and damping, respectively, defined from Ogilvie's relations (Ogilvie, 1964), as follows:

$$\begin{aligned} A_r(\omega) &= A_\infty - \tfrac{1}{\omega}\int_0^{+\infty} k_r(t)\sin(\omega t)dt, \\ B_r(\omega) &= \int_0^{+\infty} k_r(t)\cos(\omega t)dt. \end{aligned} \tag{2}$$

Thus, the radiation convolution kernel can be described, in the spectral domain, as follows:

$$H_r(\omega) = B_r(\omega) + \jmath\omega\left[A_r(\omega) - A_\infty\right], \tag{3}$$

where $k_r(t)$ and $H_r(\omega)$ are a Fourier transform pair. Using Eq. (3), Eq. (1) can be expressed in the frequency domain, considering a torque-to-angular-velocity description (Falnes, 2002), as:

$$\dot{\Theta}(\omega) = \frac{1}{Z_i(\omega)}\left[\mathcal{T}(\omega) - \mathcal{T}_u(\omega)\right], \tag{4}$$

where, for the sake of simplifying the understanding of this article, and to maintain consistency with the introduced notation in Eq. (1), the symbol $\dot{\Theta}(\omega)$ in Eq. (4) represents the Fourier transformation of the angular velocity $\dot{\theta}$, while

$$Z_i(\omega) = B_r(\omega) + \jmath\omega\left(I + A_r(\omega) - \frac{s_h}{\omega^2}\right), \tag{5}$$

denotes the mechanical impedance of the system.

The mapping in Eq. (5) can also be represented in terms of a transfer function (García-Violini, Peña-Sanchez et al., 2020), which is given by:

$$G(s) = \left.\frac{s}{s^2(I + A_\infty) + s\hat{H}_r(s) + s_h}\right|_{s=\jmath\omega} \approx \frac{1}{Z_i(\omega)}, \tag{6}$$

where $H_r(\omega)$ is typically calculated using boundary-element methods, such as NEMOH (LHEEA & NEMOH-Presentation, 2017). Furthermore, a parametric approximation to $\hat{H}_r(s) \approx H_r(\omega)$, for $s = \jmath\omega$, with $\hat{H}_r(s)$ a stable LTI system, can be computed from the radiation damping and added mass frequency-domain coefficients using advanced system ID software, such as e.g. FOAMM (Faedo, Peña-Sanchez, & Ringwood, 2018).

Equivalently, using an appropriate change of variable in Eq. (1), and a corresponding approximation for the radiation system, the WEC system can be described in a state-space form, i.e. in the time-domain, as follows:

$$\begin{cases} \dot{x}(t) = Ax(t) + B(\tau(t) - \tau_u(t)), \\ y(t) = Cx(t), \end{cases} \tag{7}$$

where the triple of matrices $(A, B, C^\intercal) \in \mathbb{R}^{n\times n} \times \mathbb{R}^n \times \mathbb{R}^n$ follows accordingly.

It is important to note that the spectral and time domain representations, described in Eqs. (6) and (7), respectively, both obtained in continuous time, can be represented using discrete time equivalents using, for example, zero- or first-order-hold discretisations (see e.g. Goodwin, Graebe, Salgado, et al. (2001)). By way of example, the discrete-time state space representation for (7) can be expressed as:

$$\begin{cases} x[k+1] = A_d x[k] + B_d(\tau[k] - \tau_u[k]), \\ y[k] = C_d x[k], \end{cases} \tag{8}$$

where $k$ is the discrete time index ($t = kt_s$), with sampling period $t_s$, and $A^d$, $B^d$, and $C^d$ refer to the discretised versions of the matrices $A$, $B$, and $C$, respectively, in Eq. (7). By way of example, the zero-order-hold equivalent (Goodwin et al., 2001), is:

$$A_d = e^{At_s}, \quad B_d = \int_0^{t_s} e^{A\zeta}B d\zeta, \quad \text{and} \quad C_d = C. \tag{9}$$

Thus, the discrete-time spectral domain is denoted by the variable $z$, which, given by the Z-transform, represents the discrete equivalent to the variable $s$.[1]

## 3. Model (In)validation

The process commonly labelled as model validation depends on the modelling framework used. Traditional validation methods describe uncertainty in a system as an additive stochastic noise with certain assumptions (Ljung, 1999), such as decorrelation and Gaussian behaviour. Model validation, in such cases, involves testing whether the actual mismatch conforms to these assumptions, and whether the noise is uncorrelated with the input (Smith et al., 1997). Additive stochastic noise models are used in open-loop problems, such as filtering and prediction (see, for example, Peña-Sanchez, Garcia-Abril, Paparella, and Ringwood (2018) and Schoen, Hals, and Moan (2011)), while perturbation models are better suited to closed-loop problems with unmodelled dynamics. When attempting to experimentally explain an observed result in a robust control oriented framework, there may be an infinite number of consistent noise signal and perturbation (dynamical uncertainty) pairs, assuming decorrelation between the input and the noise. However, finding only one pair of 'sufficient small size' for the bounds (perturbation and noise) would suffice to demonstrate that the model is still valid. Conversely, to demonstrate that the model is invalid, it is necessary to establish a lower bound on the size of any signal $d$ and perturbation $\Delta$, that accounts for the experimental dataset (Smith et al., 1997). In essence, model validation provides a way to determine whether a model is suitable for its intended purpose. If a model is invalidated, it is necessary to reconsider the identification and modelling steps. Thus, to sum up, model invalidation is a methodology to develop a robust control oriented model, which involves system analysis and understanding, physical modelling and identification, while minimum bounds (perturbation and noise) for invalidation can be analytically computed. The main features of model validation and invalidation are summarised in Table 1 (see for example Smith et al. (1997)).

### 3.1. Foundations of model invalidation

The essence of model invalidation is to verify the consistency of a given model, with its main hypotheses, and experimental datasets. The dataset comprise input and output measures, labelled as $u[k]$ and $y[k]$, respectively, where $k = 1, \ldots, N$ represents the discrete-time index. To quantify deviations between the model output and the experimental data, the system, within this context, can be described by a nominal discrete-time model $G_o(z)$, a dynamical uncertainty bound, and an output disturbance $d[k]$, as shown in Fig. 1. Thus, the general model, can be analytically represented as follows:

$$\mathcal{G} = \left\{G_o(1 + W_\Delta\Delta),\ \Delta \in \boldsymbol{\Delta}\right\}, \tag{10}$$

[1] From now on, the dependence on $s$ or $z$, i.e. continuous and discrete spectral domains, is dropped when clear from the context.

**Table 1**
Comparison between validation and invalidation of dynamical models.

| | Model validation | Model invalidation |
|---|---|---|
| Goal | To verify and confirm that a model is accurate and reliable. To assess the accuracy of a model based on a finite number of experiments | To identify flaws or inconsistencies in a model. To find a single experiment that is not consistent with the model assumptions. |
| Outcome | The model is confirmed to be valid and reliable for its intended use. The model is considered valid if it passes the validation test. | The model is shown to be invalid and needs to be revised or replaced. The model is considered invalidated if it fails the validation test. |
| Approach | A series of experiments and tests are performed to assess the model's performance. Based on classical system identification methods with additive noise. | A single experiment that produces inconsistent results is used to invalidate the model. May require perturbation models to account for unmodelled dynamics. |
| Suitability | Model validation is appropriate for models that are expected to be accurate and reliable. Well suited to open-loop problems such as filtering, estimation, and prediction. | Model invalidation is appropriate for models that may have flaws or inconsistencies that need to be identified. Better suited to closed-loop problems. |
| Result implications | A validated model can be confidently used for its intended purpose. | An invalidated model may not be suitable for its intended purpose and may require further revision or replacement. |
| Related fields | System identification, physical modelling, control theory. | Fault detection, data consistency checks, refinement of identification and modelling steps. |
| Timeframe | Model validation is typically performed during the development phase of a model. | Model invalidation can occur at any time during the model's lifecycle. |
| Number of experiments | Multiple experiments are typically performed to validate a model. | A single experiment is sufficient to invalidate a model. |

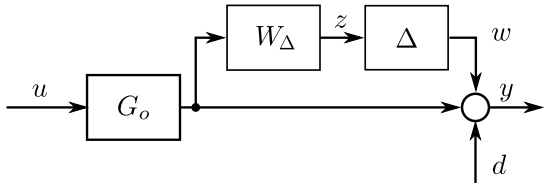


**Fig. 1.** Model block diagram for a general linear structure with a dynamical uncertainty and external noise.

where $\boldsymbol{\Delta}$ is a set of stable transfer functions, defined as $\boldsymbol{\Delta} = \{\Delta \in \mathcal{H}_\infty : \|\Delta\|_\infty \leq 1\}$, where $\mathcal{H}_\infty$ is the set of stable transfer functions with appropriate dimensions, while the infinite norm operator for systems is defined as $\|\Delta\|_\infty = \sup_{\omega\in\mathbb{R}}|\Delta(\jmath\omega)|$, for continuous time, although an equivalent discrete time formulation is also possible (Sanchez-Peña & Sznaier, 1998). The stable transfer function $W_\Delta$ in Eq. (10) represents the uncertainty dependence on frequency (as a weighting function), such that

$$\|W_\Delta \Delta\|_\infty \leq \delta. \tag{11}$$

Equivalently, the disturbance $d$ is defined as an element of the following set:

$$\mathcal{D} = \{d \in l_2(\mathcal{I}) : \|d\|_2 \leq d_{\max}\}, \tag{12}$$

where $\mathcal{I} = \{1, \dots, N\} \subset \mathbb{N}$, $\|d\|_2 = \sqrt{\sum_{k\in\mathcal{I}} d_k^2}$ denotes the energy of the discrete-time signal (i.e. sequence) $d$. Notably, this framework is particularly useful for designing robust controllers, such as $\mathcal{H}_\infty$-based controllers for LTI, LPV, and even switched systems (Bianchi & Sánchez-Peña, 2010a). From now on, given a finite sequence $d = \{d_k\}_{k\in\mathcal{I}}$, we define an associated vector $\mathbf{d} \in \mathbb{R}^N$ accordingly, i.e.

$$\mathbf{d} = \begin{bmatrix} d_1 & \dots & d_N \end{bmatrix}^\intercal. \tag{13}$$

Note that, if $d \in \mathcal{D}$, then it is straightforward to show that $\mathbf{d} \in \mathcal{D}_N$, with

$$\mathcal{D}_N = \{\mathbf{d} \in \mathbb{R}^N : \|\mathbf{d}\|_2 \leq d_{\max}\}, \tag{14}$$

where $\|\mathbf{d}\|_2 = \sqrt{\mathbf{d}^\intercal\mathbf{d}}$, with the same $d_{\max}$ as in (12).

### 3.2. Toeplitz form

A Toeplitz matrix is a matrix where each descending diagonal from left to right contains identical elements. This family of matrices is particularly useful to compute input–output interactions in dynamical systems (particularly LTI and LPV systems) using standard products of matrices.

*Definition*

Consider a sequence $h = \{h_k\}_{k\in\mathcal{I}}$, with $h_k \in \mathbb{R}$. Then the Toeplitz form of $h$ (corresponding to its associated vector $\mathbf{h}$) is:

$$T_{\mathbf{h}} = \begin{bmatrix} h_1 & 0 & 0 & \dots & 0 \\ h_2 & h_1 & 0 & \dots & 0 \\ h_3 & h_2 & h_1 & \dots & 0 \\ \vdots & \vdots & \vdots & \ddots & \vdots \\ h_N & h_{N-1} & h_{N-2} & \dots & h_1 \end{bmatrix}. \tag{15}$$

In particular, when the sequence $h$ is related to the impulse response of a general system $G$, with state matrices $A_{\mathrm{d}}$, $B_{\mathrm{d}}$, $C_{\mathrm{d}}$, and $D_{\mathrm{d}}$, the Toeplitz form of this impulse response is given by:

$$T_G = \begin{bmatrix} D_{\mathrm{d}} & 0 & 0 & \dots & 0 \\ C_{\mathrm{d}}B_{\mathrm{d}} & D_{\mathrm{d}} & 0 & \dots & 0 \\ C_{\mathrm{d}}A_{\mathrm{d}}B_{\mathrm{d}} & C_{\mathrm{d}}B_{\mathrm{d}} & D_{\mathrm{d}} & \dots & 0 \\ \vdots & \vdots & \vdots & \ddots & \vdots \\ C_{\mathrm{d}}A_{\mathrm{d}}^{n-2}B_{\mathrm{d}} & C_{\mathrm{d}}A_{\mathrm{d}}^{n-3}B & C_{\mathrm{d}}A_{\mathrm{d}}^{n-4}B & \dots & D_{\mathrm{d}} \end{bmatrix}. \tag{16}$$

It is important to note that, in Eq. (8), the feedthrough matrix $D_{\mathrm{d}}$ is zero while, in Eq. (16), it is defined in a generalised form.

*Interactions*

Based on the properties of Toeplitz matrices, the input–output interactions depicted in Fig. 1 can be expressed through the following equations:

$$\begin{aligned} T_{\mathbf{z}} &= T_{W_\Delta} T_G T_{\mathbf{u}}, \\ T_{\mathbf{y}} &= T_{\mathbf{w}} + T_G T_{\mathbf{u}} + T_{\mathbf{d}}, \\ T_{\mathbf{w}} &= T_\Delta T_{\mathbf{z}}, \end{aligned} \tag{17}$$

with $T_{W_\Delta}$, $T_G$, and $T_\Delta$ denoting the Toeplitz matrices of the impulse responses of $W_\Delta$, $G_o$, and $\Delta$, respectively. The Toeplitz matrices $T_{\mathbf{u}}$, $T_{\mathbf{y}}$, $T_{\mathbf{d}}$, and $T_{\mathbf{w}}$, in Eq. (17), represent the vectors $\mathbf{u}$, $\mathbf{y}$, $\mathbf{d}$, and $\mathbf{w}$, respectively, associated with each corresponding discrete time sequence in Fig. 1 (see also Eq. (13)).

#### 3.2.1. Model invalidation

Considering Fig. 1, if there exist vectors $\mathbf{w}$ and $\mathbf{d}$ that satisfy the constraints in Eqs. (11) and (12), respectively, the model set given by $\mathcal{G}$ is not invalidated by the experimental data provided by vectors $\mathbf{u}$ and $\mathbf{y}$. In other words, if no perturbation and disturbance signals

exist that produce an output signal consistent with the measured data, while satisfying Eqs. (11) and (12), the model is invalid. In cases where such signals do exist, the model uncertainty and noise sets are not invalidated by the existing data. Using the Schur complement (Zhang, 2006), in conjunction with Eqs. (17), (11), and (12), the invalidation of the model in Fig. 1 can be formulated as a conventional optimisation problem, with a linear objective function, constrained by linear matrix inequalities (LMIs), which can be efficiently solved using standard solvers. This optimisation problem can be stated as follows:

$$\begin{aligned} \min_{\{\mathbf{d},\mathbf{w}\}\subset\mathbb{R}^N} \quad & \tilde{f}(\delta, d_{\max}) \\ \text{s.t.} \quad & \begin{bmatrix} \left(T_{W_\Delta} T_G T_{\mathbf{u}}\right)^{\mathsf{T}} T_{W_\Delta} T_G T_{\mathbf{u}} & T_{\mathbf{w}} \\ T_{\mathbf{w}} & \delta^2 I \end{bmatrix} > 0 \\ & \begin{bmatrix} d_{\max}^2 & \mathbf{d}^{\mathsf{T}} \\ \mathbf{d} & I \end{bmatrix} > 0, \end{aligned} \tag{18}$$

where $\mathbf{d} = \mathbf{y} - \mathbf{w} - T_G\mathbf{u}$, and $\tilde{f}(\delta, d_{\max})$ denotes the objective function. In particular,

$$\tilde{f}(\delta, d_{\max}) = \alpha_\delta \delta + \alpha_d d_{\max}, \tag{19}$$

where $\alpha_\delta$ and $\alpha_d$ are positive tuning constants. In particular, if $\alpha_\delta$ ($\alpha_d$) is set to zero, the optimisation is solely performed over $\alpha_d$ ($\alpha_\delta$), while $\alpha_\delta$ ($\alpha_d$) is given in the LMI-based formulation in Eq. (18) as a known fixed parameter, rather than an unknown optimisation variable. Thus, *a-priori* information on the system and process are required to define $\alpha_\delta$ or $\alpha_d$ as known fixed variables in the optimisation problem (or process). The optimisation problem presented in Eq. (18) can be solved using standard LMI solvers, such as YALMIP (Löfberg, 2004, 2023), alongside SeDuMi (Sturm, 1999), as considered for this study.

### 3.3. Practical considerations

It should be noted that the optimisation problem described in Eq. (18) depends on obtaining output signals from convolution kernels and input signals, as shown in Eq. (17). However, this approach assumes zero initial conditions, which can lead to significant deviations between simulated and experimental data. To account for the impact of initial conditions on the comparison between simulated and experimental data, this study proposes a modification of the objective function by introducing the initial condition as a new optimisation variable in the set of LMIs. To this end, the error between *simulated* and experimental data is expressed as:

$$\mathbf{e} = \mathbf{y} - \mathbf{H}_G x_0 - T_G\mathbf{u}, \tag{20}$$

where,

$$\mathbf{H}_G = \begin{bmatrix} C_{\mathrm{d}} \\ C_{\mathrm{d}} A_{\mathrm{d}} \\ C_{\mathrm{d}} A_{\mathrm{d}}^2 \\ \vdots \\ C_{\mathrm{d}} A_{\mathrm{d}}^{n-1} \end{bmatrix} \tag{21}$$

and $x_0 \in \mathbb{R}^n$ is a new optimisation variable, denoting the unknown initial condition of the system.

Assuming $\mathbf{e}_1$ is the initial element of the truncated error signal $\mathbf{e}$, i.e. the error signal at the initial discrete time index, another set of LMIs can be added to the original problem in Eq. (18), as follows:

$$-\epsilon < \mathbf{e}_1 < \epsilon, \tag{22}$$

where $\epsilon$ denotes an additional LMI optimisation variable. Then, the final objective function is expressed as:

$$f(\delta, d_{\max}) = \alpha_\delta \delta + \alpha_d d_{\max} + \epsilon. \tag{23}$$

The modified objective function optimises both $\delta$ and $d_{\max}$, while simultaneously estimating the initial condition $x_0$.

Note that introducing additional optimisation variables for unknown initial conditions has a minimal impact on the complexity of the problem. The primary drivers of complexity are the unknown vectors $\mathbf{d}$ and $\mathbf{w}$ (typically contributing variables on the order of magnitude of 10–100), while accounting for the dimension of the state vector ($n$) for initial conditions adds only moderate complexity (additional variables on the order of magnitude of 1–10). Moreover, in most cases, particularly when working with randomly selected sections of long experiments, as in Section 5 of this study, assuming known initial conditions is not feasible.

Thus, to summarise the methodology for verifying the experimental consistency between a nominal model plus an uncertainty model with a set of experimental data (i.e., to test invalidation), the process involves the utilisation of the optimisation problem presented in Eqs. (18), (20), and (23). Solving this optimisation problem yields optimal (minimum) values for $\delta$, $d_{max}$, and $x_0$, and the corresponding vectors $\mathbf{d}$ and $\mathbf{w}$. When the LMIs are feasible, it indicates that consistency can be assured using, at least, the optimal (minimum) bounds obtained from the LMI-based optimisation problem. Conversely, when the optimisation is infeasible, it implies that there are no possible bounds for $\delta$, $d_{max}$, and $x_0$, under the considered assumptions, that can guarantee consistency.

## 4. Experiment design for input–output acquisition in WEC systems

The methodology for acquiring input–output pair data in WEC systems involves a two-step process. Firstly, the system motion is blocked and, using a force sensor, a fixed-body experiment is conducted to measure the excitation force, which serves as the input signal. Secondly, using a motion (position) sensor, a free-body experiment is carried out to measure the WEC motion, which represents the output signal. Both experiments use the same wave realisation, meaning that they have the same time trace. To ensure synchronisation, an initial trigger signal (pulse) is employed, indicating the precise moment the wave is launched in both experiments. It is important to note that this methodology differs from signal acquisition in general engineering applications, where input and output signals are typically acquired simultaneously. In this study, the assumptions of linear potential flow theory, commonly employed in the field of WECs, are adhered to. These assumptions support the consistency of the excitation force measurement with the fixed-body experiment (García-Violini et al., 2021). However, it is important to acknowledge that, in extreme sea conditions, beyond the scope of this study, the fixed-body experiment may be subject to limitations, due to potential nonlinear hydrodynamic effects. These effects could necessitate the development of a more intricate modelling framework. Considering a WEC system with angular motion, with regard to the prototype considered for the experimental assessment shown in Section 5, the introduced two-step methodology for WEC systems, is depicted in Fig. 2, with the first and second stage tests illustrated in the left- and right-hand panels, respectively. The described two-step experiment is not specific to any particular WEC structure or architecture. Rather, the difficulty of measuring motion and (wave excitation) torque/force simultaneously is an inherent characteristic of WEC technologies, requiring the estimation of excitation force in control systems for WECs. As described in Fig. 2, it should be noted that, in order to measure the forces experienced by the buoy due to hydrodynamic interactions, the PTO shaft is locked in position, clearly illustrated in Stage 1 of Fig. 2 with a red lock. Thus, although the back side (locking extreme) of the PTO is blocked, the forces experienced by the buoy are transmitted directly to the load cell. With multiple PTO systems, a fixed-body experiment requires simultaneously locking all the PTO subsystems while measuring the excitation force as a vectorial quantity, as elaborated in Faedo et al. (2023).

In experimental WEC applications, and mainly in laboratory applications, several external (to the WEC system or prototype) sources of uncertainty are inherent in the experiments, and can have a significant impact on measurements. One such source is the wave maker, which is responsible for generating the waves that are used to excite the WEC.

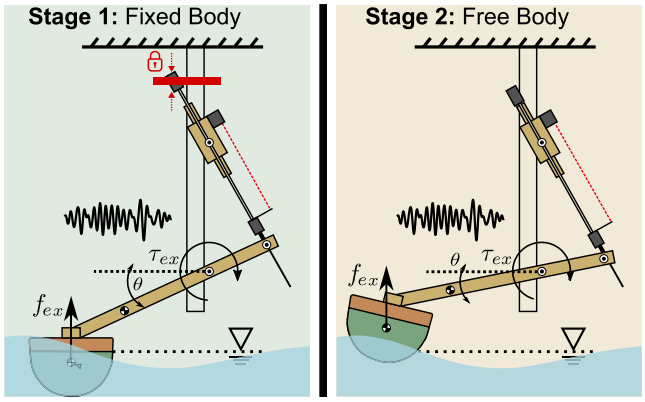


**Fig. 2.** The two-step methodology considered for WEC systems.

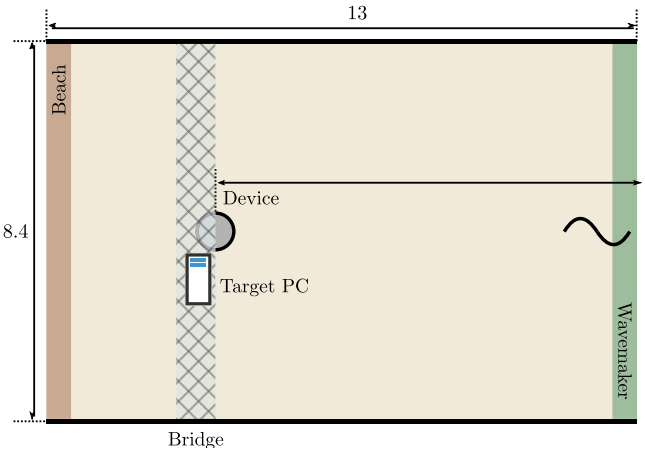


**Fig. 3.** Sketch of the wave basin in Aalborg University with the most relevant dimensions (in meters). The location of the WEC prototype is also shown. The location of the wave maker and the beach (wave absorption) is shown on the right- and left-hand side, respectively.

The wave maker accuracy and repeatability can influence the measured responses, particularly for higher-order wave spectra. Reflected waves, which are caused by wave energy reflecting back from the boundaries of the experimental tank, can also impact the measurements. Active and passive absorption techniques are often employed to reduce reflected waves; however, these mechanisms can also affect final signal acquisition. Another potentially significant source of uncertainty relates to the synchronisation trigger, relating to the (time) alignment of input and output measurements. Similarly, structural vibrations induced by the wave tank motion, or the structural platform in the tank, can also introduce additional uncertainty. While these sources of uncertainty should not be neglected, they are external to the WEC system and thus uncorrelated with the system dynamics, similar to sensor noise.

## 5. Experimental assessment of WEC systems using an invalidation method

This section discusses the results obtained from the application of the invalidation algorithms presented in Section 3.

### 5.1. Experimental setup

The experimental data used for this analysis is collected during tank tests conducted at Aalborg University in Denmark. Fig. 3 shows the most relevant dimensions of the wave basin used in the experiments. The depth of the water in the tank is 0.9 m.

The experimental setup utilised for acquiring the data is shown in Fig. 4, including a photograph and a schematic of the prototype system, on the left- and right-hand sides, respectively. This experimental infrastructure has been previously utilised in various studies, including (Ferri, Sichani, & Frigaard, 2012) and García-Violini, Peña-Sanchez, Faedo, Ferri, and Ringwood (2023). For data acquisition, a real-time software architecture is used, implemented through the Matlab/Simulink Real-Time Toolbox (version 2016b). A comprehensive description of the experimental setup including, for example, the WEC prototype, sensing and actuation systems, hardware computer and acquisition, and wave basin dimensions, can be found in García-Violini et al. (2021). It should be noted that the prototype used in this study is based on the Wave Star WEC system (Hansen & Kramer, 2011), a well-established WEC concept in the wave energy field. As shown in Fig. 4, the main hardware components involved in this study are a load cell and a laser-based position sensor, indicated in Fig. 4 with references 3 and 4. However, it must be noted that some components, such as the PTO system (1 in Fig. 4), are not directly involved in the experimental assessment presented in this study, though its dynamic response can affect the overall dynamical behaviour. Specifically, in this study, the PTO system

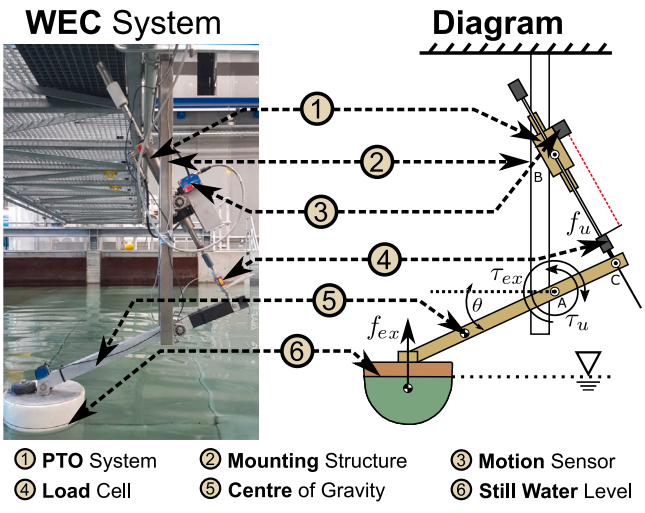


**Fig. 4.** Photograph (left) and schematic of the WEC system (right). The principal components are indicated. The bridge, illustrated in Fig. 3, is shown in the photograph.

remains inactive, distinct from its traditional role as an actuation channel in standard control problems. Nevertheless, during the free-body experiment, the PTO system can affect the general dynamic of the system. To reduce the influence of the PTO system on system dynamics, in this study, the PTO driver operates in force control mode with a 0 $N$ reference force, effectively mitigating the impact of different loading factors.

The main physical dimensions of the prototype are indicated in Table 2, where SWL and CoG represent still water level, and centre of gravity, respectively.

### 5.2. Sea-states

Four different irregular sea-states (SS1–SS4) are considered for the experimental study, as inspired by the experiments in García-Violini et al. (2021). These sea-states are generated using a JONSWAP spectral

**Table 2**
Dimensions, relative to the still water level (SWL), and mass properties for the 1/20th scale Wavestar device.

| Parameter | Value | [Unit] |
|---|---|---|
| Arm mass | 1.157 | [kg] |
| Arm MoI (at CoG) | 0.0606 | [kg m$^2$] |
| Float mass | 3.075 | [kg] |
| Float MoI (at CoG) | 0.001450 | [kg m$^2$] |
| Float diameter (at SWL) | 0.256 | [m] |
| Float draft | 0.11 | [m] |

**Table 3**
Significant wave heights ($H_s$) and peak periods ($T_p$) of the four considered sea states.

| Sea state | $H_s$ [m] | $T_p$ [s] |
|---|---|---|
| SS1 | 0.0520 | 1.836 |
| SS2 | 0.1042 | 1.836 |
| SS3 | 0.0625 | 1.412 |
| SS4 | 0.1042 | 1.412 |

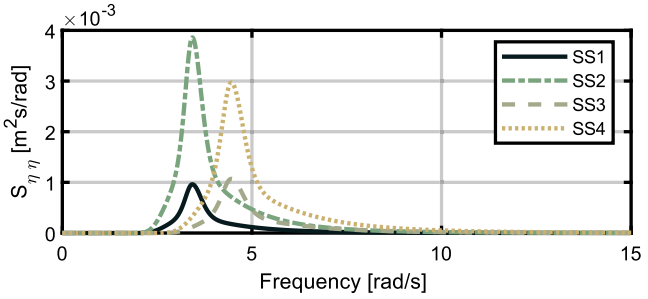


**Fig. 5.** Spectral power density for sea states SS1 to SS4.

density function with a peak shape parameter of $\gamma = 3.3$ (Hasselmann, 1973). Table 3 lists the significant wave heights ($H_s$) and peak periods ($T_p$) of the four considered sea-states. The energy content of the sea-states is determined by their power spectral density functions, denoted by $S_{\eta\eta}^{1-4}(\omega)$ for SS1–SS4, respectively. Fig. 5 shows the average (theoretical) power spectral density of the sea-states.

### 5.3. Data acquisition

One 350 s realisation is considered for each sea-state, with data acquisition performed with a sampling frequency $f_m = 1$ kHz. Fig. 6 shows a close-up of the acquired data between 110 and 125 s, which shows that the system dynamics are well covered with the considered sampling frequency. Acquired values of excitation torque, $\tau$, and angular velocity, $\dot{\theta}$, are shown (respectively) in the upper and bottom plots in Fig. 6. It is important to note that, as generally considered in control problems for WEC systems, the system velocity (angular in this study) is considered in this study as the system output.

Note that data acquisition with 1 kHz ensures effective and accurate capture of the system dynamics. However, to guarantee a tractable optimisation problem, downsampling is used to reduce the amount of data, while preserving the key system dynamics (this is discussed in Section 5.6). In addition, a 350-second experiment duration, also considered in similar studies (e.g., García-Violini et al. (2021)), achieves high statistical consistency, even with one sea state realisation.

### 5.4. Nominal models

For this study, the standard torque-to-velocity mapping, defined as follows:

$$G_i(s) = \frac{\dot{\Theta}_i(s)}{\mathcal{T}_i(s)} \tag{24}$$

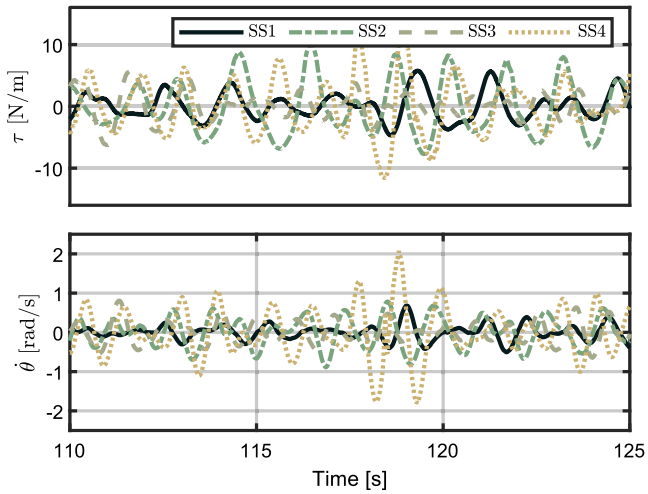


**Fig. 6.** Input and output signal acquisition for typical realisations of SS1 to SS4.

is considered, where $\dot{\Theta}_i(s)$ and $\mathcal{T}_i(s)$ are the Laplace transforms of the system angular velocity ($\dot{\theta}(t)$), and wave excitation torque ($\tau(t)$), respectively. Using standard model definition methodologies throughout the WEC literature, three nominal models are considered, labelled as $G_1(s)$, $G_2(s)$, and $G_3(s)$. Firstly, considering the same guidelines outlined in, for example, García-Violini, Peña-Sanchez et al. (2020), a model based on system identification methods is considered, identified as $G_1(j\omega)$. In order to obtain this model, a set of experiments is conducted where the fluid–structure interaction is studied using different input chirp signals, with sufficient spectral content and adequate amplitude. The excitation signals (synthesised via the control force), are applied through the PTO channel, in the absence of waves, i.e. the wavemaker is inactive. The interested reader is referred to García-Violini, Peña-Sanchez et al. (2020) for a complete discussion about the system identification methodology considered for the computation of $G_1(j\omega)$. Secondly, system $G_2(j\omega)$ is obtained following a standard first-principles modelling procedure based on Cummins' Equation (see Eq. (1)), where the radiation system is computed using BEM-based software (NEMOH for this study (LHEEA & NEMOH-Presentation, 2017)), and the main structural dimensions presented in Table 2 (see for example Davidson, Giorgi, and Ringwood (2013)). One key point to highlight is that the most widely used approach for obtaining nominal models is via Cummins' Equation and the associated general hydrodynamic modelling assumptions, as documented in the literature and performed for the computation of $G_2(j\omega)$. Finally, as generally performed in practice, $G_3(j\omega)$ is obtained by applying an *'ad-hoc'* correction of the moment of inertia $I$ in $G_2$, originally obtained from NEMOH, to achieve a better overall fit (see for example Davidson, Giorgi, and Ringwood (2015)). The frequency-responses of $G_1$, $G_2$, and $G_3$ are illustrated in Fig. 7. A noteworthy aspect is that, when manually tuning the inertia in $G_3$, a good match is achieved between $G_1$ and $G_3$ above the system resonance frequency, but there is also a good fit below the resonance frequency between $G_1$ and $G_2$. It is noteworthy that the methodologies considered for characterising systems $G_2(j\omega)$ and $G_3(j\omega)$ are widely used in the literature for wave energy conversion (WEC) systems, whereas the approach employed for $G_1(j\omega)$ is not commonly utilised. Nonetheless, the model for $G_1(j\omega)$ can incorporate dynamic effects beyond hydrodynamical interactions, such as PTO dynamics. It is important to note that the (linearising) assumption for the Cummins' model is that there are infinitesimally small variations in position/velocity (modelling paradox (Windt et al., 2021)), while the model resulting in $G_1$ is specific to the amplitude of oscillation used (see Farajvand, García-Violini et al. (2023)). For a detailed discussion on the identification and modelling-based methodologies in WEC systems, the interested reader is referred to Davidson et al. (2013, 2015) and García-Violini, Peña-Sanchez et al. (2020).

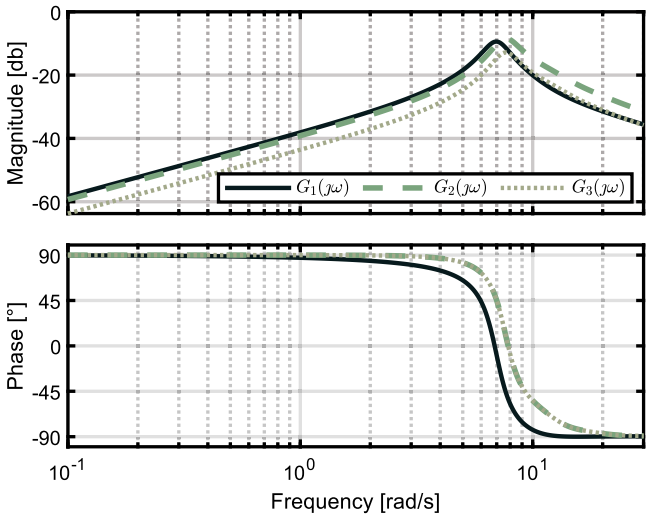


**Fig. 7.** Frequency responses of the three considered nominal models.

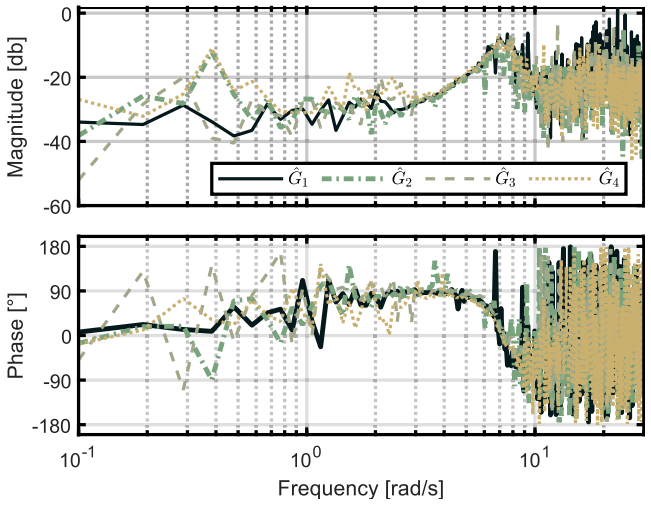


**Fig. 8.** ETFE for SS1-4.

### 5.5. ETFE and uncertainty estimation

To experimentally characterise the system, a set of empirical transfer function estimates (ETFEs) is computed using the acquired input–output pairs, obtained from all the fixed- and free-body wave-based tests. For each sea-state (indexed as $i = 1, 2, 3$, and 4), the excitation torque input $\tau_i(t)$, and the corresponding angular velocity output $\dot{\theta}_i(t)$, are used to define the set of ETFEs as:

$$\hat{G}_i(\omega) = \frac{\dot{\Theta}_i(\omega)}{\mathcal{T}_i(\omega)}, \tag{25}$$

where $\dot{\Theta}_i(\omega)$ and $\mathcal{T}_i(\omega)$ are the Fourier transforms of the system's angular velocity ($\dot{\theta}(t)$), and wave excitation torque ($\tau(t)$), respectively. An important consideration is that, in this study, ETFEs are denoted by the hat symbol $\wedge$, e.g. $\hat{G}_i$, while the nominal systems, i.e. $G_{1-3}$, are not (no $\wedge$). Moreover, for the sake of simplifying the understanding of this document and to maintain consistency with the introduced notation, the symbol $\dot{\Theta}$ in Eq. (25) represents the Fourier-transformed of the angular velocity $\dot{\theta}$, introduced in Eq. (1), rather than the derivative in the frequency spectrum. Here, $\omega \in \mathbb{R}$ represents the angular frequency in rad/s. Fig. 8 shows each ETFE, evaluated from the measured data. The ETFEs show lower variance (*'cleaner'* behaviour) within the range of significant spectral content provided by the incident waves, which is approximately between 2 and 6 rad/s (see also Fig. 5). In addition, in Fig. 8, beyond the frequency with significant frequency content, the responses are noisy, with no defined trend. In Fig. 8, unfiltered raw data previews, underlining the motivation for conducting an invalidation analysis to select the best WEC model, are provided. Importantly, the curves in Fig. 8 do not influence the invalidation procedure presented in this study. Furthermore, for a stochastic description and analysis of the results in Fig. 8, cross-correlation-based analysis can be employed, although this is beyond the scope of this study. The erratic amplitude behaviour observed before 2 rad/s, and after 6 rad/s, in Fig. 8 is generated by several factors, including PSD variability introduced by stochastically synthesised excitation torques derived from filtered white noise. Additionally, the low-frequency amplitude responses are particularly affected by FFT resolution (inversely proportional to the experiment length). It is essential to emphasise that the observed peak at 0.4 rad/s for $G_2$ and $G_4$ does not signify specific system dynamics. Additionally, despite the apparent smoothness of signals in Fig. 6, these signals, derived from filtered white noise for synthesising irregular waves, exhibit quasiperiodic patterns that significantly influence the denominator of Eq. (25), particularly during minimal system motion. The two-step experiments introduce external disturbances such as reflections, refractions, and synchronisation issues, further impacting the spectral content in Fig. 8.

Thus, based on the three nominal models considered, $G_1(s)$, $G_2(s)$, and $G_3(s)$, and each ETFE, $\hat{G}_i(j\omega)$ , with $i = \{1, 2, 3, 4\}$, the general uncertainty nature can be estimated. To that end, based on the experimental responses and considering the multiplicative structure presented in Fig. 1, the uncertainty set can be approximated as follows:

$$|\Delta(\omega)| = \max_{i,j} \left| \frac{G_j(j\omega) - \hat{G}_i(\omega)}{G_j(j\omega)} \right|, \tag{26}$$

with $i = \{1, 2, 3, 4\}$ and $j = \{1, 2, 3\}$. Eq. (26) is a well-established definition commonly used to describe systems with added multiplicative uncertainty, especially within the framework of robust control (see, for example, Sanchez-Peña and Sznaier (1998)). It provides a standard way to quantify the relative difference between the nominal transfer function and the experimental transfer function. The result of applying Eq. (26) can be found in Fig. 9. It is important to note that Fig. 9 presents two distinct scenarios. Firstly, from a cursory examination of Fig. 8, it is evident that there is significant variability in the high-frequency part of the spectrum. While this variability could be due to dynamic processes, at this stage of the study it is impossible to distinguish between exogenous noise and dynamic uncertainty. Secondly, an increase in uncertainty can be observed at lower frequencies, which can be attributed to the numerical limitations of the Fourier transform, implemented using a well-established FFT algorithm. Therefore, an infinite-length experiment would be required to achieve good low frequency resolution. Furthermore, a high level of confidence can be assumed for the lower frequency dynamics, as null velocity is obtained if a constant force is applied to the system ($\omega \to 0$ rad/s), due to elementary interactions, such as a spring-damper dynamic (buoyancy and radiation). This implies relatively complete knowledge for $\omega = 0$ rad/s.

To address the uncertainty estimation features mentioned in the previous paragraphs, in accordance with the structure presented in Fig. 1, five different uncertainty weighting functions are considered, labelled as $W_\Delta^k(s)$ with $k \in \{1, 2, 3, 4, 5\}$. Specifically, four of these weighting functions indicate the high frequencies for dynamic uncertainty, while at low frequencies, each $W_\Delta^k(s)$ assigns greater significance to external noise. Additionally, a unitary weighting function, $W_\Delta^4(s)$, is included to evenly distribute the same level of influence/importance to both noise and dynamic perturbation. The sigma plots (magnitude of the frequency response) of each $W_\Delta^k(s)$ are illustrated in Fig. 10.

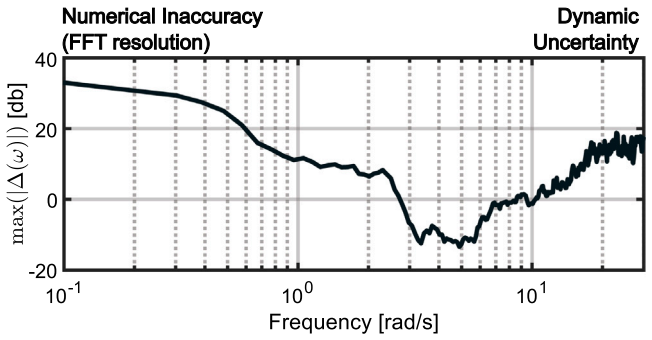


**Fig. 9.** Uncertainty estimation based on the considered nominal models and the computed ETFE.

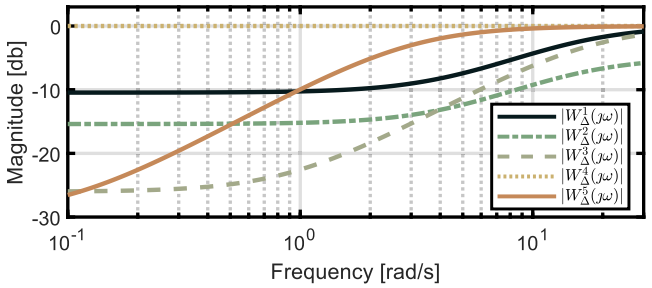


**Fig. 10.** Magnitude of the frequency response of each $W_{\Delta}^{k}(s)$.

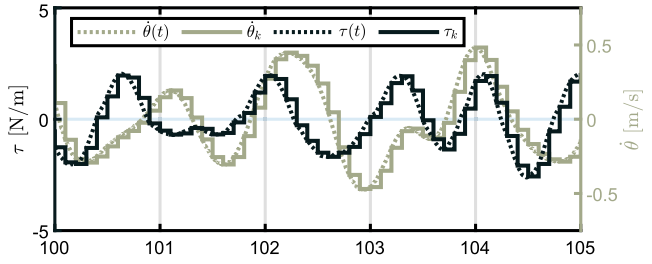


**Fig. 11.** Downsampling procedure applied to both the excitation torque and system velocity.

### 5.6. Model invalidation setup

In order to apply the methodologies discussed in Section 3, two important considerations must be made. Firstly, it should be noted that the acquired signals have a sampling rate of $f_m = 1$ kHz, which makes the application of LMI-based algorithms, in particular for model invalidation, impractical, due to the excessive number of data points. To address this issue, a downsampling procedure is applied to obtain a more tractable data set size. Specifically, a downsampling factor of 100 is used, resulting in an effective sampling rate of $f_m^e = 10$ Hz $= 20\pi$ rad/s. Notably, this reduction in sampling rate does not affect the integrity of the procedure, as both the typical wave frequencies (inverse of typical period $T_p$) and nominal system resonance frequencies are significantly below 10 Hz (1 Hz approximately). Fig. 11 shows a comparison between the original acquisition and the subsequently downsampled signals for both the excitation torque and the system velocity.

To prepare the signals for the LMI-based procedure presented in Eq. (18), and to make the most of the large amount of available data, this study analyses the complete set of data using a sliding window of length 10 s. The window is used to scroll through all the data from $t = 0$ s to $t = 340$ s, which is the total length of the data minus the window length. Thus, for each iteration, i.e. sliding window position, the set

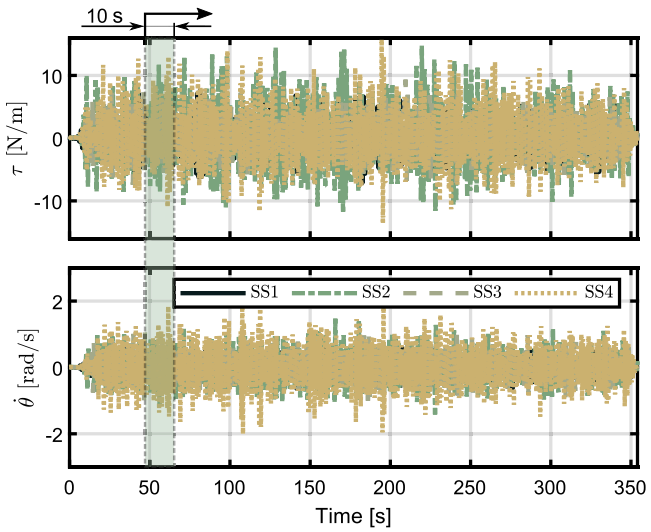


**Fig. 12.** General methodology for the application of the presented invalidation procedure.

of LMIs presented in Eq. (18) is solved. The general methodology is illustrated in Fig. 12 for all the sea-states, where the sliding window is indicated with a shadowed-area.

### 5.7. Model invalidation results

The set of LMIs in Eq. (18) is solved using the objective function presented in Eq. (23). Since there is no estimation or *a-priori* knowledge of external noise sources, i.e. measurement noise, reflections, and/or inaccuracies in the wave maker (see Section 4), in this study, five LMI optimisation variables, i.e. signals $w$ and $d$, the bounds $\delta$ and $d_{\max}$, and the initial condition $x_0$, as presented in Fig. 1 and Eqs. (18) and (23), are considered in the optimisation problem, to achieve the smallest norm of parameters that does not invalidate the experiments and models, i.e. verify experimental consistency. Thus, as an engineering criterion, dynamical uncertainty is weighted 10 times more than uncorrelated external factors which, in analytical terms, is achieved using $\alpha_\delta = 0.1$ and $\alpha_d = 1$, as presented in Eq. (23). It should be noted that the analysis includes a total of 204,000 cases, taking into account the three nominal models, five uncertainty weighting functions, four sea-states, and 3400 positions for the sliding windows (with 3500 samples per time trace and 100 samples per sliding window). Thus, for each optimisation run, a set of five variables is obtained:

$$\left\{\delta^*, \quad d^*_{\max}, \quad \mathbf{w}^*, \quad \mathbf{d}^*, \quad x_0^*\right\}, \tag{27}$$

where $\delta^*$, $d^*_{\max}$, $\mathbf{d}^*$, $\mathbf{w}^*$, $x_0^*$ denote the optimal values obtained by solving the set of LMIs in Eqs. (18) and (23), to optimally guarantee model and experimental consistency.

By way of example, the results of applying the proposed methodology, considering $G_1(s)$, SS1–SS2, and $W_{\Delta}^{5}(s)$, are shown in Fig. 13 using a dispersion plot, where each individual circular marker represents the solution, in terms of $\delta^*$ and $d^*_{\max}$, for one sliding window. The results in Fig. 13 show the obtained optimal values of $\delta^*$ and $d^*_{\max}$ for each location of the sliding window, i.e. 3400 locations, with the results for SS1 and SS2 presented on the left- and right-hand side, respectively. At first glance, the results in Fig. 13 suggest that the dispersion level for SS2, which is a more energetic sea-state compared to SS1, is large. This observation indicates the interconnection between displacement demand and uncertainty level in WEC systems, as discussed in Section 1 (see Windt et al. (2021)).

In Fig. 14, the time traces obtained from the invalidation procedure, $\mathbf{w}^*$ and $\mathbf{d}^*$, are shown, along with the input and output signals,

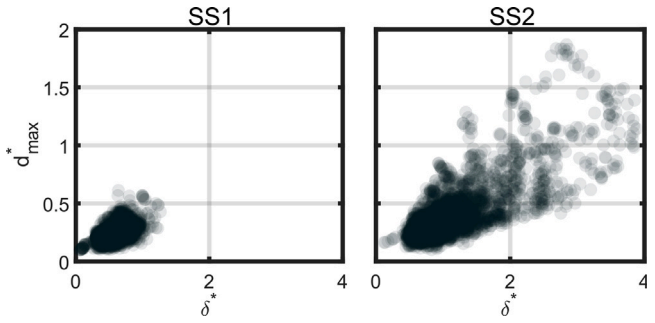


**Fig. 13.** Dispersion analysis on the obtained optimal values for $\delta^*$ and $d_{\max}$, with $G_1(s)$, $W_\Delta^5$, and SS1 (left) and SS2 (right).

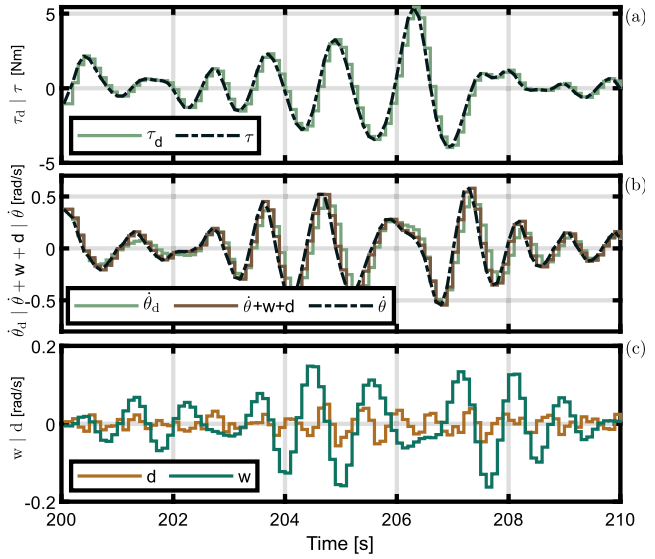


**Fig. 14.** Input (a) and output (b), and perturbation and noise (c) time traces obtained with $G_1(s)$, $W_\Delta(s)$ and $SS1$. (For interpretation of the references to colour in this figure legend, the reader is referred to the web version of this article.)

considering $G_1(s)$, SS1, and $W_\Delta^5(s)$, as an example. Specifically, the top (a), middle (b), and bottom (c) plots in Fig. 14 correspond to the input signal (excitation torque, in [Nm] ), output signal (angular velocity, [rad/s]), and perturbation and noise (external signals, in [rad/s]), respectively. In Fig. 14(a), the dashed-black and green-solid lines correspond to the excitation torque signal $\tau$, acquired using $f_m = 1$ kHz, and the downsampled excitation torque signal $\tau_d$, obtained using $f_m^e = 10$ Hz, respectively. In Fig. 14(b), the dashed-black line indicates the system velocity $\dot{\theta}$, acquired with $f_m = 1$ kHz, the solid-green line denotes the discrete-time nominal angular velocity $\dot{\theta}_d$, synthesised using $\tau$ and the discrete version of $G_1(s)$, while the solid-brown line illustrates the angular velocity reconstruction obtained by adding $\dot{\theta}_d$ and the obtained perturbation, $w$, and noise, $d$, signals. Finally, in Fig. 14(c), the discrete time traces of the obtained perturbation signal, $w$, and the exogenous noise, $d$, are shown using green and brown solid lines, respectively. Additionally, note that reconstruction of the experimental output by adding $\dot{\theta}_d$, $w$, and $d$ signals provides evidence that the assumptions made in Eq. (18) are verified. Furthermore, upon examination of Fig. 14(c), and comparing the magnitudes of $d$ and $w$, it is evident that the noise level is considerably lower than the perturbation level, thus satisfying the design requirement described in Section 5.7.

As an additional verification step, considering $G_1(s)$, SS1, and $W_\Delta^5(s)$, in Fig. 15, the time traces obtained for $w$ (top) and $d$ (bottom) are shown for two sliding windows shifted by 4 s, i.e. 200–210 s and

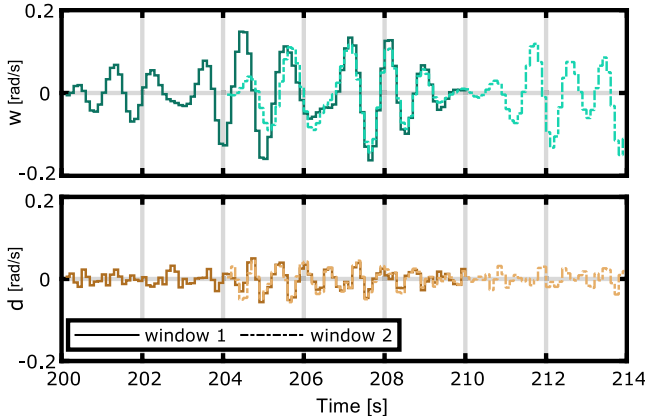


**Fig. 15.** Analysis of perturbation and noise signals obtained with two sliding windows shifted 4 s. (For interpretation of the references to colour in this figure legend, the reader is referred to the web version of this article.)

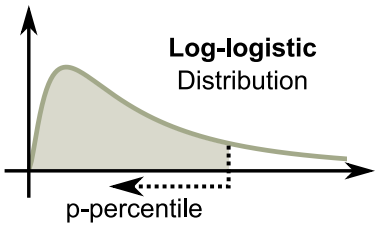


**Fig. 16.** General behaviour of a log–logistic distribution and the percentile of value p.

204–214 s. In Fig. 15, dark and light coloured lines indicate the results for window 1 (200–100) and window 2 (204–214), respectively, while the colours for $w$ and $d$ are green and brown, respectively, in agreement with the colour code considered for the bottom plot of Fig. 14. Note that, in Fig. 15, the initial conditions for both perturbation and noise, i.e. $w$ and $d$, are set to zero by the optimisation process, as there are no available estimates, unlike the nominal system, which utilises the optimisation variable $x_0$ to estimate the initial condition of the system. However, from an overall perspective, it should be noted that there is an approximate convergence time of 1 s between the results obtained for each sliding window (from 204 s to 205 s), indicating consistency of the algorithm.

To take advantage of the large amount of data obtained, as a consequence of the extended duration of the experimental tests, in this study, a statistical interpretation of the invalidation results is performed. To this end, a histogram-based analysis is utilised. Specifically, a set of histograms is generated by counting the number of occurrences of each optimal solution for $\delta^*$ and $d^*_{\max}$, for each particular position of the sliding window. This procedure is performed for each nominal model, uncertainty weighing function, and sea-state. Furthermore, a sufficient number of bins is considered in order to obtain good approximation of a continuous statistical distribution. In particular, without loss of generality, the log-logistic statistical distribution is used to approximate the results obtained in the histograms, in accordance with the asymmetric nature of the results. The selection of the log-logistic distribution is not based on specific physical justification, but rather on an examination of various statistical distributions, including, for example, the Rayleigh distribution. The log-logistic distribution was chosen due to its better fit to the obtained histograms. In Fig. 16, the general behaviour of a log-logistic statistical distribution is shown. In contrast to, for example, a normal distribution, Fig. 16 highlights the non-symmetric shape of a log-logistic distribution.

Fig. 17 presents the histogram analysis for the results of $\delta^*$ and $d_{\max}$ and their log-logistic approximations, obtained from the analysis of SS1

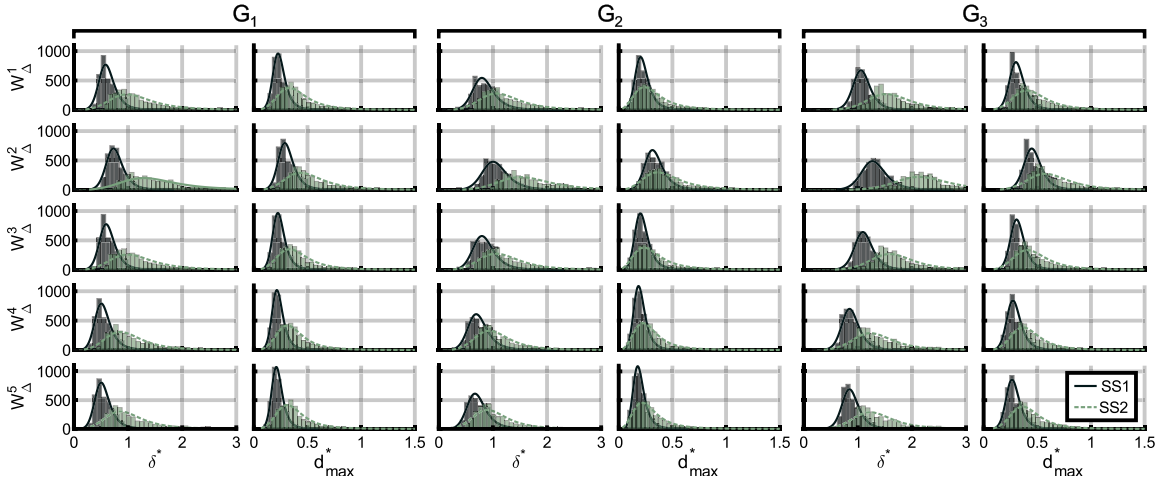


**Fig. 17.** Histogram analysis for the results of $\delta^*$ and $d_{\max}$ for SS1 and SS2, considering $G_{1-3}$ with $W_\Delta^{1-5}$. (For interpretation of the references to colour in this figure legend, the reader is referred to the web version of this article.)

and SS2, illustrated using black bars and solid-black line (distribution), and green bars and dashed-green line (distribution), respectively. The analysis in Fig. 17 is conducted using $G_1$-$G_3$ in conjunction with $W_\Delta^1$-$W_\Delta^5$. As mentioned for the results in Fig. 13, it can be noted that, in general, more uncertainty and noise levels are estimated for SS2, which is the most energetic sea-state under analysis in Fig. 17. Furthermore, $W_\Delta^5$ which, in accordance with the assumptions discussed in Section 5.5 is the weighting function with the lowest magnitude for $\omega \mapsto 0$, achieves the lowest values of dynamical uncertainty, for virtually all the considered cases. In addition, it is important to note that the results obtained for SS1 exhibit a higher degree of focus (peakiness) compared to those obtained for SS2. The larger uncertainty and noise sets for SS2, resulting from the extended WEC motion, relative to SS1, account for this observation. However, despite the larger variability in SS2 results, the area enclosed by the bars (summation of the occurrences) in both cases is identical, owing to the same number of cases analysed for both SS1 and SS2.

One key point to highlight is that selecting a specific value, such as the peak location in the curves shown in Fig. 17, to define a robust control-oriented model (see Eqs. (10) and (12)), can lead to invalidation of the model assumptions for some cases, unless the maximum values of $\delta^*$ and $d^*_{\max}$ are chosen. To be more specific, for instance, if the case characterised by $G_1$ and $W_\Delta^5$ is considered, the location of the peak of the curves is at $\delta^* \approx 0.47$ and $d^*_{\max} \approx 0.20$ for SS1, and $\delta^* \approx 0.83$ and $d^*_{\max} \approx 0.30$ for SS2. However, if these values are used to define the system (as in Eqs. (10) and (12)), then any case where the obtained values of $\delta^*$ and $d^*_{\max}$ are larger would invalidate the experimental data, and the associated nominal system. However, defining a model based on the maximum obtained values for $\delta^*$ and $d^*_{\max}$, to ensure consistency with all the analysed cases, can lead to an overly conservative model which, in general, is a generic weakness of standard robust control design procedures (Sanchez-Peña & Sznaier, 1998).

In this context, this study proposes a methodology that considers percentiles of the obtained estimation for each distribution, shown in Fig. 17. As depicted in Fig. 16, the p-percentile represents the area under the curve where p% of the cases fall. Considering $W_\Delta^1$-$W_\Delta^5$, $G_1$-$G_3$, SS1-SS4, Fig. 18 shows the values obtained in the 50-percentile (top) and 90-percentile (bottom) cases, for $\delta^*$ (left) and $d^*_{\max}$ (right). In Fig. 18, each $W_\Delta^i$ is indicated with a different colour, while each nominal model is represented with a solid box, a red line, and an empty box for $G_1$, $G_2$, and $G_3$, respectively. In general, the results in Fig. 18 indicate that model $G_1$ is more adequate, compared to $G_2$ and $G_3$, in terms of reducing the uncertainty bound. However, for some cases, such as SS3, $G_2$ is more appropriate. This fact highlights the fundamental essence of the invalidation paradigm, which emphasises

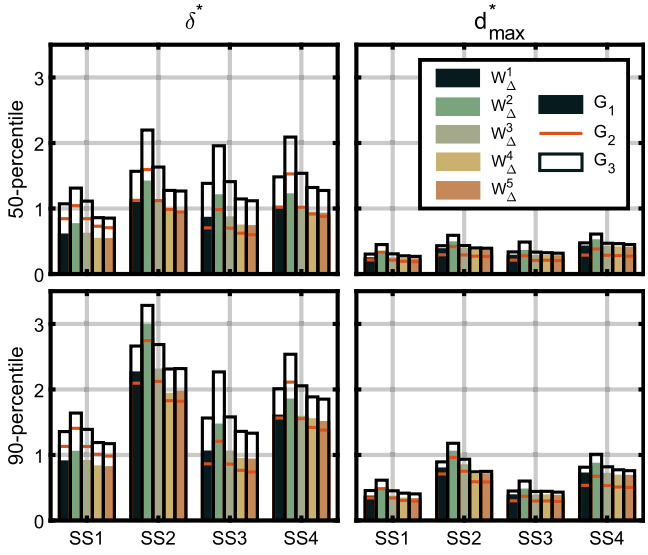


**Fig. 18.** Percentile analysis from the histogram results in Fig. 17. (For interpretation of the references to colour in this figure legend, the reader is referred to the web version of this article.)

the importance of choosing the most suitable model based on the experimental conditions. Certain features of the experiment, such as the spectral content of the input signals, can reveal certain characteristics of the models that make them more or less appropriate than others. In terms of the resulting noise bounds, model $G_2$ is generally more appropriate, although the noise bounds are significantly lower than those obtained for the uncertainty and, as previously discussed, cannot impact on closed-loop stability. From the results in Fig. 18, it can be noticed that the similarities obtained for $G_1$ and $G_2$ can be explained by the equivalent frequency response in the band below 6 rad/s, as shown in Fig. 7. In contrast, $G_3$ generally provides lower performance, in terms of $\delta^*$ and $d^*_{\max}$.

## 6. Control implications for WEC systems

This section presents an analysis of the practical implications of including uncertainty models in WEC control performance, specifically in terms of energy absorption. The analysis considers the uncertainty and external noise estimation results obtained in Section 5. Two control structures, namely a closed-loop control structure, defined as

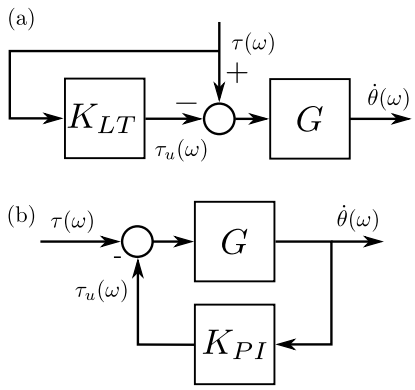


**Fig. 19.** Control structures. (a) LiTe-Con and (b) PI controller.

proportional-integral (PI) control (Falnes, 2002), and an open-loop control structure known as LiTe-Con (García-Violini, Peña-Sanchez et al., 2020; García-Violini et al., 2021), are examined. These control structures, due to the nature of the loop architectures that implement them, highlight different characteristics of models with dynamical uncertainty. The interested reader is referred to Falnes (2002) and García-Violini et al. (2021) for a detailed discussion about the controller structures PI and LiTe-Con, respectively. In this study, both control schemes are described from an overall perspective. In Fig. 19 (a) and (b), the LiTe-Con and PI control schemes are shown, respectively. It is important to note that the implementation of LiTe-Con requires an estimate of the wave excitation torque. However, for the purpose of this study, perfect knowledge of the wave excitation torque is assumed, without loss of generality, to focus on the essence of the analysis technique. A variety of estimators for wave excitation torque/force is available, with the interested reader referred to Peña-Sanchez, Windt, Davidson, and Ringwood (2019). Note that, in this study, the excitation torques, $\tau_1$-$\tau_4$, corresponding to each sea-state, are acquired using a fixed body experiment. This assumption does not affect the implications or conclusions drawn in this study. Additionally, narrow-banded and broad-banded control solutions (power absorption) are achieved with the PI and LiTe-Con control schemes, respectively.

For this study, no motion constraints are considered. In addition, to simplify the analysis and reduce the number of cases, only the combination of SS1-SS4 with the associated $\tau_1$-$\tau_4$, $G_1$ as nominal system, and $W_\Delta^5$, are considered. Nevertheless, this selection of cases does not affect the analysis, as the observations made from this case can be generalised and applied beyond this illustrative case.

Based on the uncertainty and noise bound estimates in Section 5.7 for the 50-percentile case, presented in Figs. 17 and 18, a family of models with dynamic uncertainty is built for $G_1(1 + \Delta W_\Delta^5)$, as shown in Fig. 20, where the nominal system and 240 (60 cases for each sea-state) models, given by the uncertainty definition corresponding to each sea-state, are illustrated using dashed-green and grey lines, respectively. For generating the families of models, the distribution results and bounds in Fig. 17, for the case considered, are used.

### 6.1. LiTe-Con

Using a frequency-domain system identification algorithm (Faedo et al., 2018), the LiTe-Con approximates the optimal control condition for the feedforward controller $H^{opt}(\omega)$, given by the impedance-matching condition (Falnes, 2002), with a LTI-stable and implementable dynamical system $K_{LT}(s)$, i.e.:

$$K_{LT}(s)\Big|_{s=j\omega} \approx H^{opt}(\omega), \tag{28}$$

for $\omega \in [\omega_l, \omega_u]$, which represents the target frequency band for the controller approximation, consistent with the spectral content of the waves. Then, the resulting control torque can be defined, in the frequency domain, as follows:

$$\mathcal{T}_u(\omega) = K_{LT}(j\omega)\mathcal{T}(\omega). \tag{29}$$

With the definition in Eq. (28), the resulting torque-to-velocity mapping is:

$$T^{LT}_{\tau\mapsto\dot{\theta}}(j\omega) = \left(1 - K_{LT}(j\omega)\right) G(j\omega), \tag{30}$$

for $\omega \in [\omega_l, \omega_u]$. The LiTe-Con provides a broadband control solution to effectively deal with panchromatic sea-states, where the power spectral density is mainly contained within $[\omega_l, \omega_u]$. The interested reader is referred to García-Violini, Peña-Sanchez et al. (2020) for a detailed discussion on LiTe-Con.

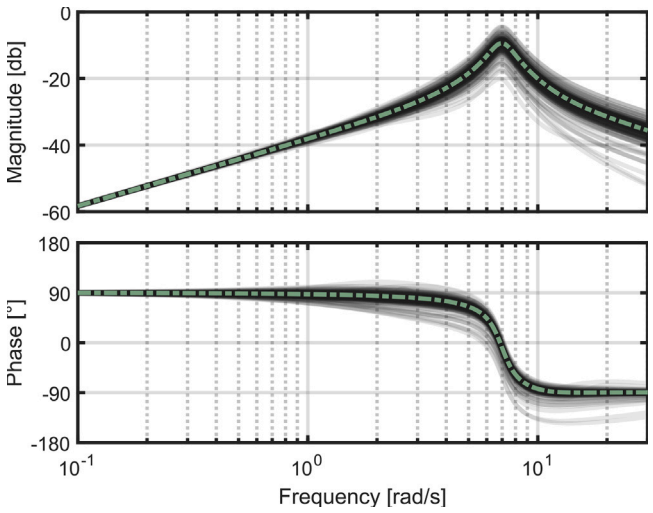


**Fig. 20.** Family of models for $G_1(1 + \Delta W_\Delta)$. The nominal model and the family of models are shown using green and grey lines. (For interpretation of the references to colour in this figure legend, the reader is referred to the web version of this article.)

### 6.2. PI control

The PI controller represents a well-established standard feedback control solution within the WEC control literature. The control torque is computed as a standard linear combination of position and velocity of the WEC system:

$$\tau_u(t) = \begin{bmatrix} k_p & k_i \end{bmatrix} \begin{bmatrix} \theta(t) \\ \dot{\theta}(t) \end{bmatrix}, \tag{31}$$

which, using standard properties of the Laplace transform, can be written as

$$K_{PI}(s) = \frac{k_p s + k_i}{s}, \tag{32}$$

while the representation of the control torque in the frequency domain is given by:

$$\mathcal{T}_u(\omega) = K_{PI}(j\omega)\dot{\Theta}(\omega). \tag{33}$$

The resulting torque-to-velocity mapping is:

$$T^{PI}_{\tau\mapsto\dot{\theta}}(j\omega) = \frac{G(j\omega)}{1 + G(j\omega)K_{PI}(j\omega)}. \tag{34}$$

Based on the impedance-matching condition (see Falnes (2002)), analytical conditions can be given to maximise the absorbed energy, in unconstrained scenarios with monochromatic waves or a representative single frequency (e.g. the frequency corresponding to the peak of

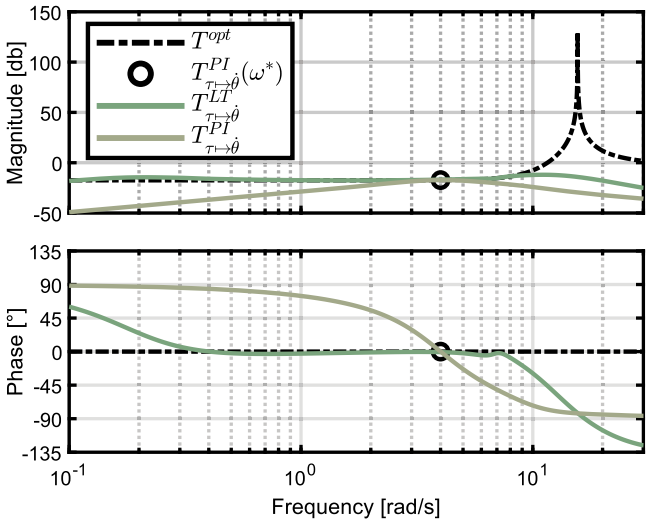


**Fig. 21.** Torque-to-velocity mapping obtained with the designed PI and LiTe-Con controllers.

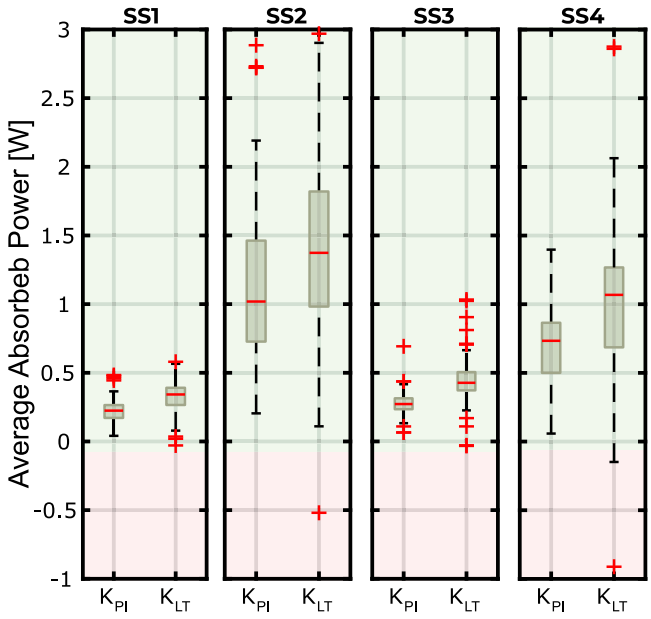


**Fig. 22.** Dispersion analysis of the average absorbed power.

the wave spectrum) in a panchromatic sea. Thus, the PI controller parameters can be computed as follows,

$$k_p = \mathbb{R}e\left\{\Phi(\omega^*)\right\}, \quad k_i = -\omega^* \mathbb{I}m\left\{\Phi(\omega^*)\right\} \tag{35}$$

with $\mathbb{R}e$ and $\mathbb{I}m$ the real and imaginary part operators, where

$$\Phi(\omega^*) = \frac{1}{T^{opt}_{\tau\mapsto\theta}(\omega^*)} - \frac{1}{G(j\omega^*)}, \tag{36}$$

and $\omega^*$ is a particular frequency (e.g. the peak wave frequency), where the energy absorption maximisation is targeted. Thus, the impedance-matching condition is satisfied for $\omega^*$ with $K_{PI}(s)$.

### 6.3. Control performance

In the context of WEC systems, the effectiveness of energy maximising controllers is typically evaluated based on the absorbed energy. Mathematically, the absorbed energy $E$ over a time interval $[0, T]$ with $T \in \mathbb{R}^+$ can be represented as the integral of the instantaneous mechanical absorbed power $P_{abs}(t)$, as:

$$E = \int_0^T P_{abs}(t)dt = \int_0^T \dot{\theta}(t)\tau_u(t)dt \tag{37}$$

where $P_{abs}(t)$ denotes the instantaneous mechanical absorbed power. The discrete-time case can be obtained by replacing the integral in Eq. (37) with a summation. In particular, in this study, $T = 350$ s (the experiment length), with the performance of each controller is evaluated based on the average absorbed power:

$$\bar{P}_{abs} = \frac{E}{T}, \tag{38}$$

which provides a statistically consistent measure of the absorption behaviour, taking into account the long duration of the time traces for SS1-4.

### 6.4. Control results

The final torque-to-velocity mapping obtained with each control scheme is shown in Fig. 21. In particular, for the PI controller $\omega^*$ is 4 rad/s, as the representative single frequency in accordance with the typical periods of the sea-states in Table 3. In Fig. 21, it can be noted that each controller approaches the optimal condition, $T^{opt}$, with the LiTe-Con achieving a wider power absorption bandwidth compared with the PI controller.

As a consequence of considering dynamic uncertainty in the model, the most remarkable result is in relation to closed-loop stability, in the $K_{PI}$ case. As $K_{PI}$ is designed only for the nominal model, using Eq. (35), there are no guarantees of robust stability, as guaranteed in $H_\infty$-based controllers, such as mixed sensitives or loop-shaping (Sanchez-Peña & Sznaier, 1998).

When examining the family of models presented in Fig. 20, it must be mentioned that, for the models generated for SS1, SS2, SS3, and SS4, 0%, 25%, 6.7%, and 20% of cases, respectively, resulted in an unstable closed-loop, i.e. 0, 15, 4, and 12 cases for SS1, SS2, SS3, and SS4, respectively. As a result, the power absorption calculation, presented in the following, cannot include the performance of such unstable closed-loop cases.

The power absorption obtained for $K_{LT}$ and $K_{PI}$, with SS1-4, is shown in Fig. 22. The central mark of each box on the subplots (SS1-4) in Fig. 22 denotes the median, while the lower and upper box edges represent the 25th and 75th percentiles, respectively. The extensions to each box (above and below), show the most extreme data points that are not considered outliers, while the outliers are represented by individual data points marked with a + symbol, defined as in The MathWorks (2021).

It can be noted, from Fig. 22, that a larger variation is obtained with $K_{LT}$, compared with the variation obtained with $K_{PI}$. In general, a larger value of mean absorbed power is obtained with the LiTe-Con; however, in some cases, the LiTe-Con absorbs energy from the grid instead of providing it, mainly for SS2 and SS4, which are the most energetic sea states (largest uncertainty bounds). This undesirable characteristic of WEC energy *consumption*, has been also reported in Garcia-Violini and Ringwood (2021) for a WEC model with uncertainty, although considering a spectral-based control strategy. Note that the larger absorption capability of $K_{LT}$ is due to its broadband nature. In addition, it is important to note that, even though the $K_{PI}$ controller always provides positive power, a number of unstable cases have been removed from the analysis. Thus, the results shown in Fig. 22 indicate that, without considering uncertainty in the dynamical models, overestimation in performance can be obtained in the final performance assessment.

Note that existing literature has often prioritised the maximisation of power absorption through different control methodologies, sometimes without due consideration for the essential aspect of closed-loop stability. This work aims to underscore the significance of this critical issue. Future developments in control must prioritise the creation of controllers that can simultaneously guarantee optimal energy maximisation and robust stability. Therefore, it is imperative for the reader to recognise that a model incapable of predicting instability should be avoided when considering applications in, for example, control.

## 7. Conclusion

Firstly, this study presents a methodology for building input–output data sets in wave energy converters (WECs), based on a two stage methodology. Secondly, a model invalidation methodology is presented for WEC systems that is capable of separately analysing dynamical uncertainty and external noise in the experimental data sets. The presented invalidation methodology analyses the results from a statistical point of view, which leads to a less conservative analysis framework, relative to standard results throughout the literature for model invalidation. The practical implications of considering dynamic uncertainty in the models of WEC systems are discussed in terms of control performance, specifically the absorbed energy. The study reveals that failure to include dynamic uncertainty in the analysis may generate performance overestimation. The importance of having a good dynamic description to achieve accurate estimates of experimental control performance is primarily highlighted in this study. Furthermore, this study underscores the need for closed-loop controllers for WEC systems that simultaneously pursue energy maximisation and guarantee robust stability, which is currently unavailable in the WEC literature.

In conclusion, the presented study provides a new and practical framework for addressing the issue of dynamic uncertainty in WEC systems. The study highlights the importance of incorporating this type of uncertainty in the analysis of WEC control performance to avoid overestimation of energy capture performance.

## Declaration of competing interest

The authors declare that they have no known competing financial interests or personal relationships that could have appeared to influence the work reported in this paper.

## Acknowledgements

This material is based upon works supported byScience Foundation Ireland (SFI) through the MaREI Centre for Energy, Climate and Marine under Grant No. 12/RC/2302 P2. In addition, this project has received funding from the European Union's Horizon 2020 research and innovation programme under the Marie Sklodowska-Curie grant agreements N° 101024372, N° 731084, and N° 101034297. The author would like to acknowledge Demián García-Violini has been financially supported by the Agencia I+D+i with the PICT-2021-I-INVI-00190 grant. Conflict of interest - none declared.

## References

Anderson, J., & Papachristodoulou, A. (2009). On validation and invalidation of biological models. *BMC Bioinformatics*, *10*(1), 1–13.

Beven, K., & Lane, S. (2019). Invalidation of models and fitness-for-purpose: A rejectionist approach. *Computer Simulation Validation: Fundamental Concepts, Methodological Frameworks, and Philosophical Perspectives*, 145–171.

Bianchi, F. D., Moscoso-Vásquez, M., Colmegna, P., & Sánchez-Pena, R. S. (2019). Invalidation and low-order model set for artificial pancreas robust control design. *Journal of Process Control*, *76*, 133–140.

Bianchi, F. D., & Sánchez-Peña, R. S. (2010a). A novel design approach for switched LPV controllers. *International Journal of Control*, *83*(8), 1710–1717.

Bianchi, F. D., & Sánchez-Peña, R. S. (2010b). Robust identification/invalidation in an LPV framework. *International Journal of Robust and Nonlinear Control*, *20*(3), 301–312.

Cummins, W. E. (1962). The impulse response function and ship motions. *Schiffstechnik*, *47*, 101–109.

Davidson, J., Giorgi, S., & Ringwood, J. V. (2013). Linear hydrodynamic modelling for wave energy devices using system identification techniques. In *Proceedings of the 10th European wave and tidal energy conference*. Aalborg, Denmark.

Davidson, J., Giorgi, S., & Ringwood, J. V. (2015). Linear parametric hydrodynamic models for ocean wave energy converters identified from numerical wave tank experiments. *Ocean Engineering*, *103*, 31–39.

Faedo, N., Peña-Sanchez, Y., Pasta, E., Papini, G., Mosquera, F. D., & Ferri, F. (2023). SWELL: An open-access experimental dataset for arrays of wave energy conversion systems. *Renewable Energy*, *212*, 699–716.

Faedo, N., Peña-Sanchez, Y., & Ringwood, J. V. (2018). Finite-order hydrodynamic model determination for wave energy applications using moment-matching. *Ocean Engineering*, *163*, 251–263.

Falnes, J. (2002). *Ocean waves and oscillating systems: linear interactions including wave-energy extraction*. Cambridge Univ. Press.

Farajvand, M., García-Violini, D., & Ringwood, J. V. (2023). Representative linearised models for a wave energy converter using various levels of force excitation. *Ocean Engineering*, *270*, Article 113635. http://dx.doi.org/10.1016/j.oceaneng.2023.113635.

Farajvand, M., García-Violini, D., Windt, C., Grazioso, V., & Ringwood, J. V. (2021). Quantifying hydrodynamic model uncertainty for robust control of wave energy devices. In *14th European wave and tidal energy conference-EWTEC*.

Farajvand, M., Grazioso, V., García-Violini, D., & Ringwood, J. V. (2023). Uncertainty estimation in wave energy systems with applications in robust energy maximising control. *Renewable Energy*, *203*, 194–204. http://dx.doi.org/10.1016/j.renene.2022.12.054.

Ferri, F., Sichani, M. T., & Frigaard, P. (2012). A case study of short-term wave forecasting based on FIR filter: Optimization of the power production for the wavestar device. In *The twenty-second international offshore and polar engineering conference*. OnePetro.

García-Violini, D., Faedo, N., Jaramillo-Lopez, F., & Ringwood, J. V. (2020). Simple controllers for wave energy devices compared. *Journal of Marine Science and Engineering*, *8*(10), 793.

García-Violini, D., Peña-Sanchez, Y., Faedo, N., Ferri, F., & Ringwood, J. V. (2023). A broadband time-varying energy maximising control for wave energy systems (LiTe-Con+): Framework and experimental assessment. *IEEE Transactions on Sustainable Energy*, 1–10. http://dx.doi.org/10.1109/TSTE.2023.3237023.

García-Violini, D., Peña-Sanchez, Y., Faedo, N., & Ringwood, J. V. (2020). An energy-maximising linear time invariant controller (LiTe-Con) for wave energy devices. *IEEE Transactions on Sustainable Energy*, *11*(4), 2713–2721.

García-Violini, D., Peña-Sanchez, Y., Faedo, N., Windt, C., Ferri, F., & Ringwood, J. V. (2021). Experimental implementation and validation of a broadband LTI energy-maximizing control strategy for the wavestar device. *IEEE Transactions on Control Systems Technology*, *29*(6), 2609–2621.

Garcia-Violini, D., & Ringwood, J. V. (2021). Energy maximising robust control for spectral and pseudospectral methods with application to wave energy systems. *International Journal of Control*, *94*(4), 1102–1113. http://dx.doi.org/10.1080/00207179.2019.1632491.

Goodwin, G. C., Graebe, S. F., Salgado, M. E., et al. (2001). *Control system design, Vol. 240*. Prentice Hall New Jersey.

Guo, B., & Ringwood, J. V. (2021). A review of wave energy technology from a research and commercial perspective. *IET Renewable Power Generation*, *15*(14), 3065–3090.

Hansen, R. H., & Kramer, M. M. (2011). Modelling and control of the wavestar prototype. In *Proc. EWTEC*. Southampton, UK.

Harirchi, F., & Ozay, N. (2018). Guaranteed model-based fault detection in cyber–physical systems: A model invalidation approach. *Automatica*, *93*, 476–488.

Hasselmann, K. (1973). *Measurements of wind wave growth and swell decay during the Joint North Sea Wave Project (JONSWAP), Vol. 8* (p. 95). Deutches Hydrographisches Institut.

LHEEA, & NEMOH-Presentation (2017). Laboratoire de recherche en hydrodynamique énergetique et environnement atmospherique. https://goo.gl/yX8nFu [Online accessed 1-Aug-2019].

Livstone, M. M., Dahleh, M. A., & Farrell, J. A. (1994). A framework for robust control based model invalidation. In *Proceedings of 1994 American control conference-ACC'94, Vol. 3* (pp. 3017–3020). IEEE.

Ljung, L. (1999). *System identification - theory for the user*. Prentice Hall.

Löfberg, J. (2004). YALMIP: A toolbox for modeling and optimization in MATLAB. In *Proceedings of the symposium on computer-aided control system design* (pp. 284–289). Taipei, Taiwan.

Löfberg, J. (2023). YALMIP website. https://yalmip.github.io/ [Online accessed 24-Mar-2023].

Ogilvie, T. F. (1964). Recent progress toward the understanding and prediction of ship motions. In *5th symposium on naval hydrodynamics, Vol. 1* (pp. 2–5). Bergen, Norway.

Peña-Sanchez, Y., Garcia-Abril, M., Paparella, F., & Ringwood, J. V. (2018). Estimation and forecasting of excitation force for arrays of wave energy devices. *IEEE Transactions on Sustainable Energy*, *9*(4), 1672–1680.

Peña-Sanchez, Y., Windt, C., Davidson, J., & Ringwood, J. V. (2019). A critical comparison of excitation force estimators for wave-energy devices. *IEEE Transactions on Control Systems Technology*, *28*(6), 2263–2275.

Popper, K. (2005). *The logic of scientific discovery*. Routledge.

Ringwood, J. V., Bacelli, G., & Fusco, F. (2014). Energy-maximizing control of wave-energy converters: The development of control system technology to optimize their operation. *IEEE Control Systems*, *34*(5), 30–55.

Sanchez-Peña, R. S., & Sznaier, M. (1998). *Robust systems theory and applications*. Wiley New York.

Schoen, M. P., Hals, J., & Moan, T. (2011). Wave prediction and robust control of heaving wave energy devices for irregular waves. *IEEE Transactions on Energy Conversion*, *26*(2), 627–638.

Smith, R. (1990). *Model validation for uncertain systems* (Ph.D. thesis), California Institute of Technology.

Smith, R. S., & Doyle, J. C. (1989). Model invalidation: A connection between robust control and identification. In *1989 American control conference* (pp. 1435–1440). IEEE.

Smith, R., Dullerud, G., Rangan, S., & Poolla, K. (1997). Model validation for dynamically uncertain systems. *Mathematical Modelling of Systems*, *3*(1), 43–58.

Sturm, J. F. (1999). Using SeDuMi 1.02, a MATLAB toolbox for optimization over symmetric cones. *Optimization Methods & Software*, *11*, 625–653.

Sznaier, M., & Mazzaro, M. C. (2003). An LMI approach to control-oriented identification and model (in) validation of LPV systems. *IEEE Transactions on Automatic Control*, *48*(9), 1619–1624.

The MathWorks, I. (2021). *boxplot documentation*. Natick, MA: The MathWorks, Inc., URL https://www.mathworks.com/help/stats/boxplot.html.

Vrachimis, S. G., Timotheou, S., Eliades, D. G., & Polycarpou, M. M. (2021). Leakage detection and localization in water distribution systems: A model invalidation approach. *Control Engineering Practice*, *110*, Article 104755.

Windt, C., Faedo, N., Penalba, M., Dias, F., & Ringwood, J. V. (2021). Reactive control of wave energy devices–the modelling paradox. *Applied Ocean Research*, *109*, Article 102574.

Zhang, F. (2006). *The Schur complement and its applications, Vol. 4*. Springer Science & Business Media.